Facile preparation of MgO/graphene oxide nanocomposite for efficient removal of aqueous Congo red: adsorption performance and interaction mechanism

Ting Guo[1] · Chaoke Bulin[2]

Abstract

Aqueous dyes are important source of water pollution. In this work, a nanocomposite MgO/graphene oxide (MgO/GO) was prepared with a simple solvothermal method. The as-prepared MgO/GO was characterized and employed as a potential adsorbent to remove aqueous Congo red (CR). The interaction mechanism between MgO/GO and CR was clarified. The adsorption of CR (initial concentration 700 mg L^{-1}) onto MgO/GO (dosage 1000 mg L^{-1}) equilibrated in 10 min, adsorption percent and adsorption quantity were 97.84% and 684.85 mg g^{-1}, respectively. Compared with other adsorbents, MgO/GO was superior in adsorption efficiency due to the fast adsorption kinetics. Moreover, MgO/GO exhibited good adaptability to the fluctuations of environmental factors including CR initial concentration and coexisting electrolyte. The adsorption fits well with the Freundlich model and PSO model; chemical adsorption was the rate-controlling step. Both GO and MgO in MgO/GO contributed to CR adsorption. GO adsorbed CR via an electrostatic attraction and face-to-face π–π interaction, MgO adsorbed CR via weak van der Waals force. Owing to the advantages as facile preparation, high adsorption efficiency, and good environmental adaptability, MgO/GO may be a promising adsorbent for aqueous dyes.

Keywords Magnesium oxide · Graphene oxide · Congo red · Adsorption · Interaction mechanism

✉ Chaoke Bulin
  quan820720@126.com

1   College of Energy and Environment, Inner Mongolia University of Science and Technology, Baotou 014010, People's Republic of China

2   College of Materials and Metallurgy, Inner Mongolia University of Science and Technology, Baotou 014010, People's Republic of China

Introduction

With the rapid development of the modern industry, environmental pollution is becoming increasingly serious. Among water pollutants, organic dyestuff represents a significant proportion because of its extensive use in textile, cosmetics, food, pharmaceutical, printing, and dyeing industries [1]. Firstly, dyes spoil the esthetics of water, causing visual pollution. Secondly, dyes impede the transmission of sunlight, impacting the activities of the aquatic biota. Thirdly, aqueous dyes enter the human body via food chain to bring health problems. Congo red (CR) is an important representative of organic dyes that widely used in the textile industries. Congo red (CR) is non-degradable and carcinogenic [2], whose removal from effluent is highly concerned.

Numerous technologies including adsorption [3, 4], coagulation [5], photocatalytic degradation [6–8], and membrane treatment [9] have been employed to treat dye pollution. Among these technologies, adsorption represents a promising one due to its low cost, flexible operation, and high efficiency. Conventional adsorbents such as activated carbon, silica gel, and resin generally suffer from drawbacks such as low capacity, slow kinetics, and inadequate reusability. To overcome these drawbacks, extensive research efforts have been made to develop high-performance adsorbents based on nanostructure.

Graphene oxide (GO) is a carbonaceous material derived from graphite oxidization. The oxidation process introduces abundant oxygenous groups such as carboxyl, hydroxy, carbonyl, and epoxy. These groups are accommodated on the high specific surface area of GO to serve as anchoring sites for various water contaminants [10–13].

Nanosized metal oxides have been widely investigated in research areas such as adsorption and catalysis [14]. A most attractive one is magnesium oxide (MgO), since it is cheap, stable, non-toxic [15], and easy to prepare. However, nanoparticles tend to aggregate due to high surface energy, leading to the weakening of the adsorption efficiency. Substrate material such as GO can efficiently inhibit the aggregation of nanoparticles. Therefore, a nanocomposite based on MgO/GO framework is anticipated to make the best use of the two components.

Xu et al. [16] synthesized magnesium oxide (MgO) with a flower morphology and MgO–graphene oxide (GO) composite with MgO diameter of 500 nm. Adsorption tests indicate that the MgO–GO composite prepared with 0.5 wt % GO showed higher adsorption capacity (237.0 mg g^{-1}) than single MgO (227.7 mg g^{-1}). Electrostatic attraction plays a key interaction mechanism in adsorption. M. Nagpal et al. [17] synthesized a mesoporous magnesium oxide–graphene oxide composite using a facile post-immobilization method. The adsorption performance of the composite toward indigo carmine (IC) and orange G (OG) was investigated, and the adsorption mechanism was analyzed. Results show that the maximum adsorption capacities of the composite for IC and OG were 252.4 and 24.5 mg g^{-1}, respectively, and electrostatic interaction and hydrogen bonding contributed as the main adsorption force. Sahoo et al. [18] synthesized MgO–MgFe$_2$O$_4$/GO and MgO–Fe$_2$O$_3$ nanocomposites via the hydrothermal

method. The two nanocomposites were used as efficient adsorbents to remove aqueous fluoride ions, and the adsorption mechanism was explored. Results indicate that the maximum adsorption capacity of MgO–MgFe$_2$O$_4$/GO for fluoride ions was 34 mg g^{-1}; the adsorption mechanism involves electrostatic interactions, anion exchange, and inner-sphere complexation. Sahoo et al. [19] synthesized nanosized magnesium oxide decorated iron oxide nanorods (Fe$_2$O$_3$–MgO) via a simple one-step hydrothermal method. The as-synthesized Fe$_2$O$_3$–MgO was used as an adsorbent to eliminate aqueous Congo red (CR). The maximum adsorption capacity of 200 mg g^{-1} occurred at pH = 4, and the CR attachment on the adsorbent surface was due to electrostatic interaction. Hota et al. [20] prepared a Fe$_3$O$_4$ nanoparticle-functionalized GO/g–C$_3$N$_4$ nanocomposite using the hydrothermal method. The as-prepared nanocomposite exhibited maximum adsorption capacity of 120 mg g^{-1} for toxic tetracycline (TC) antibiotic and 220 mg g^{-1} for methylene blue (MB) dye, respectively; π–π interaction and hydrogen bonding served as interaction mechanism.

Despite these remarkable research progresses, two works are still worth doing. (1) Work at performance level. The adsorption capacity of MgO/GO system can be further improved via elaborately controlling the material preparation parameters. (2) Work at mechanism level. The interaction mechanism between MgO/GO and organic dyes may be more accurately investigated via comprehensive analyses on adsorption experiments, adsorption models, and spectroscopic measurements. Herein, a facile solvothermal method to fabricate MgO/GO nanocomposite was presented. The as-fabricated composite was characterized and employed as adsorbent to remove CR from an aqueous solution. The adsorption performance was evaluated, and the interaction mechanism between MgO/GO and CR was clarified. Results indicate that the as-fabricated MgO/GO has high adsorption efficiency toward aqueous CR. The superior performance and facile preparation may make MgO/GO a promising adsorbent for aqueous dye.

Experimental

Materials

The reagents used in this work are: natural flake graphite (325 meshes, Qingdao Meilikun Co. Ltd., China), KMnO$_4$ (Tianjin wind ship chemical reagent Co., Ltd., China), K$_2$FeO$_4$ (AR, Hubei CSW Chemistry Co., Ltd., China), H$_2$SO$_4$ (98 wt%, AR, Beijing chemical works, China), H$_2$O$_2$ (30 wt%, AR, Tianjin Huadong reagent Co, China), and deionized water. The following reagents were purchased from Beijing chemical reagent Co., China: ethylene glycol (EG), Mg(CH$_3$COO)$_2$·4H$_2$O, polyvinylpyrrolidone (PVP), Congo red (CR), HCl (37.5 wt%), NaOH. All reagents are of analytically pure.

Preparation of MgO/GO

GO was prepared via oxidizing natural flake graphite using the modified Hummers method [21]. MgO/GO was fabricated with a simple solvothermal method as follows. GO powder (0.1400 g) was put into EG (280 mL) and ultrasonicated for 15 min. Then, $Mg(CH_3COO)_2 \cdot 4H_2O$ (2.9961 g) and PVP (2.3241 g) were added simultaneously into the GO colloidal. The colloidal was then ultrasonicated for 30 min to obtain a homogeneous dispersion. The as-obtained dispersion was transferred into a Teflon-lined autoclave and subject to solvothermal reaction at 180 ℃ for 5 h. Reaction completed and the autoclave was cooled down to room temperature. The reaction product was taken out and washed with deionized water repeatedly. Finally, the washed product was vacuum-dried at 300 ℃ for 2 h to obtain MgO/GO. The fabrication process is illustrated in Scheme 1. The single MgO was fabricated with a similar procedure without the presence of GO.

Characterization methods

The phase species of the sample was identified by X-ray diffraction (XRD; PANalytical, X'Pert PRO, Netherlands). The morphological features of the sample were observed using transmission electron microscope (TEM; JEOL, JEM-2100, Japan). The functional groups of the samples were analyzed using Fourier transformation infrared spectroscopy (FTIR; Bruker, IFS66V, Germany) and ultraviolet–visible light spectroscopy (UV–Vis; HITACHI, U-3900, Japan). The surface elements were analyzed using X-ray photoelectron spectroscopy (XPS; Kratos Axis Supra, England). The mass percent of functional groups and MgO in MgO/GO was evaluated by thermogravimetry–differential thermal analysis (TG–DTA; NETZSCH, STA449C, Germany). The Barrett–Joyner–Halenda (BJH) pore volume and Brunauer–Emmett–Teller (BET) specific surface area of the sample were determined via N_2 adsorption–desorption measurements conducted under a specific surface and pore size analyzer (Micromeritics, ASAP 2020 V3.04 G, USA). The pH of the adsorbent hydrosol and adsorbate solution was monitored by a pH meter (pH; Shanghai Leici Co. Ltd., pHS-3E, China). The zeta potential of the adsorbent hydrosol under varying pH was measured by micro-electrophoresis meter (zeta potential; Shanghai Zhongchen Co. Ltd., JS94H, China).
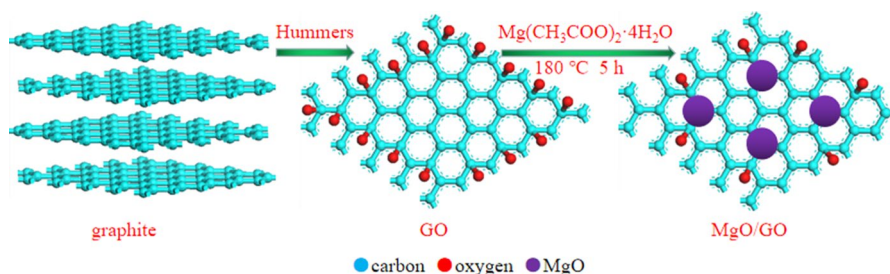
Scheme 1 Fabrication process of MgO/GO

Batch adsorptions

CR solution (20 mL, 150–700 mg L^{-1}) was put into a flask; the solution pH was adjusted to target value (2–11) using 0.1 M HCl or NaOH. A certain dosage (300–1000 mg L^{-1}) of MgO/GO was added into the flask. Then, the flask was shook in a shaker at a preset temperature (5–40 °C) to experience a certain contact time (1–10 min). Finally, MgO/GO was quickly separated via vacuum filtration to obtain a clear filtrate. The as-separated MgO/GO was washed for FTIR and UV–Vis analyses. The concentration of CR in the filtrate was determined according to the Lambert beer's law by recording solution absorbance at the wavelength of 497 nm using ultraviolet–visible light spectroscopy (UV–Vis; HITACHI, U-3900, Japan). The adsorbent dosage D (mg L^{-1}), adsorption percent R_i (%), and adsorption quantity Q_i (mg g^{-1}) are determined using Eqs. (1)–(3):

$$D = \frac{m}{V} \tag{1}$$

$$R_i = \frac{C_0 - C_i}{C_0} \times 100\% \tag{2}$$

$$Q_i = m \tag{3}$$

where $i = 0$, e, t mean the initial, equilibrium, and t moment states, respectively. C_i (mg L^{-1}) denotes the solution concentration of CR, V (mL) denotes solution volume, m (g) denotes the mass of MgO/GO. All assays were performed in duplicate, and the mean values were presented.

The non-equilibrium data C_t and Q_t with varying time intervals were fit using the pseudo-first-order (PFO), pseudo-second-order (PSO), intra-particle diffusion, liquid film diffusion, and Bangham models for kinetic analysis. The equilibrium data C_e and Q_e under a certain temperature were fit using the Langmuir, Freundlich, Temkin, and D-R models for isotherm analysis. The equilibrium data C_e and Q_e under varying temperatures were fit using Van't Hoff equation for thermodynamic analysis. The validity of the fitting results was evaluated by the correlation coefficient (R^2).

Cyclic adsorption: The CR-adsorbed MgO/GO was put into 20 mL deionized water, and the pH was adjusted to 10 (justification for desorption under pH = 10: adsorption reaches its lowest level at pH = 10–11, as shown in Fig. 8). Then, the suspension was shook for 30 min. Finally, the regenerated MgO/GO was separated for the next cycle of adsorption. Five consecutive cycles were implemented with a same procedure.

Interaction mechanism

The interaction mechanism between MgO/GO and CR was clarified via comprehensive analyses on the batch adsorptions, adsorption isotherms, kinetics, thermodynamics, and the sample spectra.

Results and discussion

Characterization of MgO/GO

Figure 1 compares the XRD patterns of MgO, GO, and MgO/GO. In the pattern of GO, the peak at 13.08° was the (001) reflection of graphene oxide [10]. In the pattern of MgO/GO, this (001) peak shifted to 10.04°. Meanwhile, a new peak appeared at 20.38°, which was assigned to the (002) reflection of reduced graphene oxide (rGO) [11]. For both MgO and MgO/GO, peaks at 37.50°, 42.50°, 59.20°, 72.04°, and 79.02° were assigned to the (111), (200), (220), (311), and (222) reflections of MgO phase, respectively [15]. The above comparison suggests the successful attachment of MgO on GO and reduction of GO.

Figure 2 shows the TEM image, HRTEM image, and SAED pattern (from left to right) of MgO/GO. In the TEM image, the angles and lines were either the edges or the folding lines of the graphene sheets. The flaky dark areas in the TEM image were the loaded MgO. The HRTEM image exhibited graphene edges and MgO flakes more clearly. No clear atomic arrays were observed in the HRTEM, implying that both the phases of graphene and MgO in MgO/GO may be poorly crystallized, as supported by the diffraction rings in the SAED pattern.

Figure 3 shows the FTIR spectra of GO and MgO/GO. Peaks at 3427 cm^{-1} and 3415 cm^{-1} in the two spectra were ascribed to the O–H stretching vibration of the -COOH group [12]. In the FTIR spectrum of MgO/GO, the $C=C$ peak (1650 cm^{-1}) and C–OH peak (1401 cm^{-1}) came from GO [13], while the Mg-OH peak (1048 cm^{-1}) came from MgO [22]. The appearance of C=C, C–OH, and Mg-OH peaks confirmed the existence of both GO and MgO in MgO/GO. Moreover, the original peaks of GO encountered some changes after the fabrication of MgO/GO: (1) The original peaks of C=O (1740 cm^{-1}), C–O–C (1242 cm^{-1}), and C–O (1079 cm^{-1}) in GO did not appear in the spectrum of MgO/GO. Nonappearance of these oxygen-containing groups in MgO/GO implied the reduction of GO during MgO/GO fabrication, which coincided with the XRD results. (2) The O–H (3427 cm^{-1}) in MgO/GO blue-shifted as compared to O–H (3415 cm^{-1})
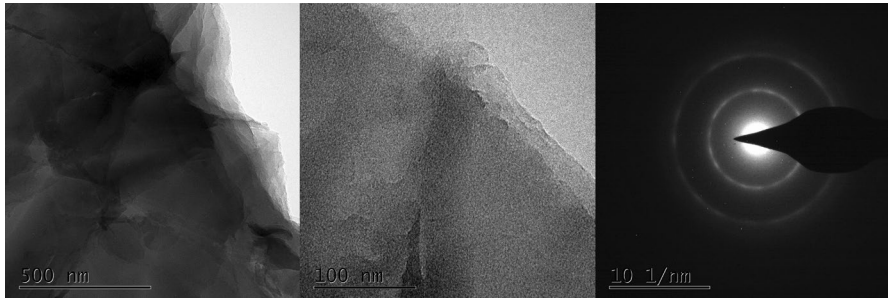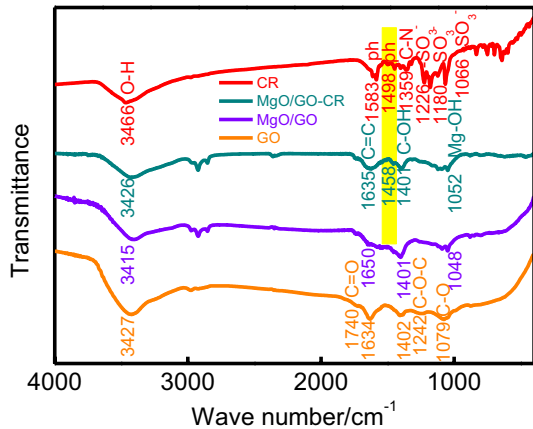
Fig. 1 XRD patterns of MgO, GO, and MgO/GO
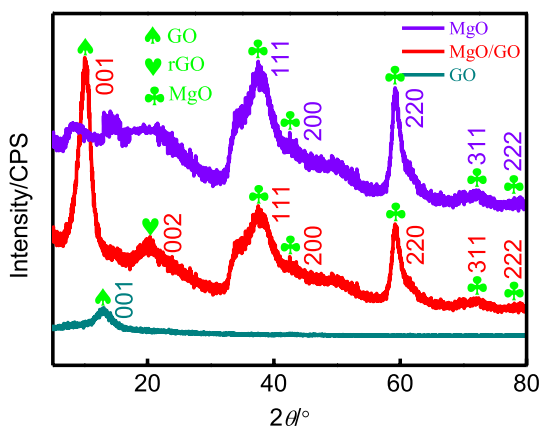
**Fig. 2** TEM images and SAED pattern of MgO/GO

Fig. 3 FTIR spectra of GO, MgO/GO, MgO/GO-CR, and CR

in GO. This shift suggested that the MgO precursor interacted with the functional groups of GO such as -COOH to form MgO in situ.

Figure 4a compares the XPS survey spectra of GO and MgO/GO. In the survey spectrum of MgO/GO, the Mg1s peak at 1300–1308 eV further confirmed the existence of Mg in MgO/GO. The inset under the green arrow shows the high-resolution Mg1s spectrum. Moreover, intensity ratios of O1s to C1s were 1.80, 0.97 for GO, MgO/GO, respectively, which indicated that graphene oxide was partially reduced during MgO/GO fabrication. To gain more insights into the reduction details, deconvolution was performed on the C1s peaks of GO and MgO/GO to get the high-resolution spectra, which are presented in Fig. 4b and c, respectively. A careful comparison revealed two differences between them: (1) difference in peak position. Three sub-peaks C=O, C–O, and C–C of GO were at 287.20, 286.56, and 284.77 eV, respectively. As for MgO/GO, these peaks were at 284.98, 284.14, and 283.67 eV, respectively. That is, the C1s peak red-shifted. Generally, electron gain brings negative valence and decreased electron binding energy (red shift) for an atom. On the contrary, electron loss brings positive valence and increased electron binding energy (blue shift) for an atom. GO

Fig. 4 a XPS survey spectra of GO and MgO/GO (inset under the cyan arrow: high-resolution Mg1s spectrum of MgO/GO), **b** high-resolution C1s spectrum of GO, **c** high-resolution C1s spectrum of MgO/GO. (Color figure online)
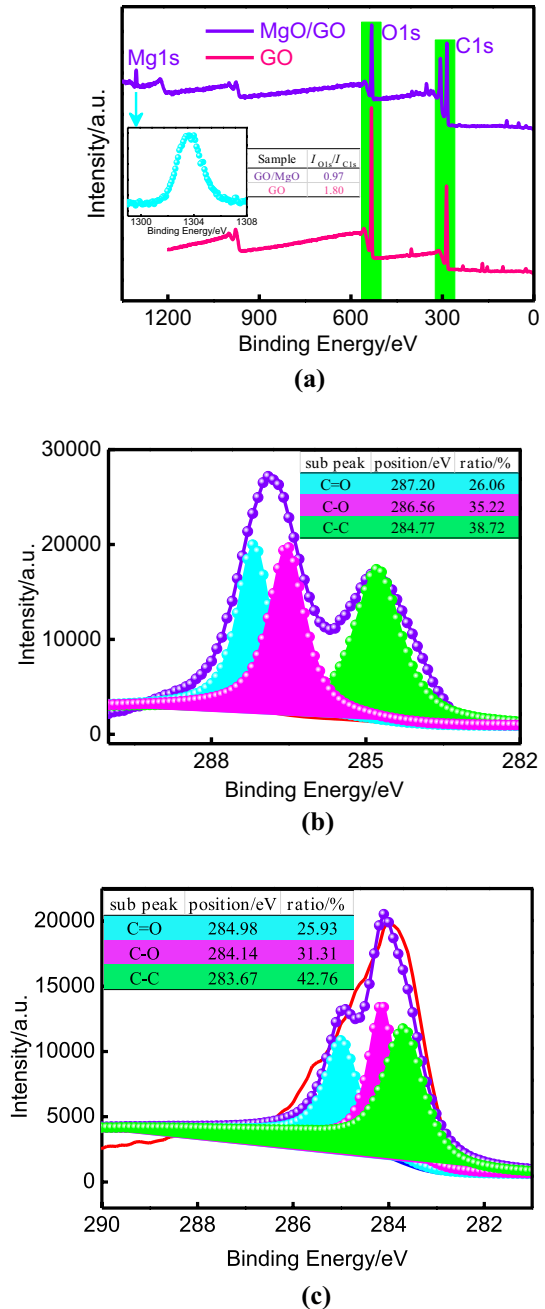
reduction removed oxygen atoms bonded to carbon atoms, as confirmed by XRD and FTIR. Since oxygen is more electronegative than carbon, the removal of oxygen atoms made the electron density of carbon atoms increase, leading to C1s red

Table 1 Orbitals and binding energies of the elements in MgO/GO

Element	C	O	Mg
Orbital	C1s	O1s	Mg1s
Binding energy/eV	284.77–287.20	528.32–534.78	1300.63–1306.69

Fig. 5 TG–DTA curves of MgO/GO
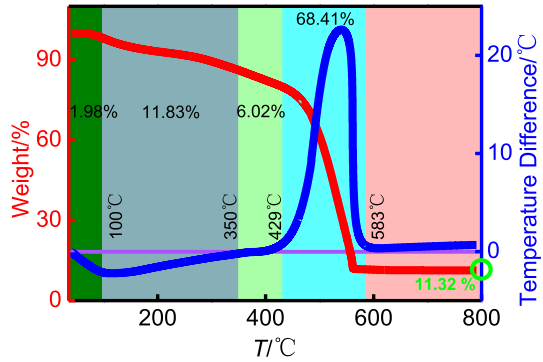
shift. (2) Difference in peak shape. The ratios of the sub-peaks C=O, C–O, and C–C of GO were 26.06, 35.22, and 38.72%, respectively. As for MgO/GO, these ratios were 25.93, 31.31, and 42.76%, respectively. Clearly, a noticeable decrease in C–O ratio and increase in C–C ratio occurred. These have two implications: (1) C–O-related functional groups such as –COOH interacted with MgO precursor during MgO/GO fabrication. (2) GO was reduced. These conclusions were consistent with those drawn from XRD and FTIR. The electron orbitals and binding energies of the elements in MgO/GO confirmed by XPS analysis are listed in Table 1.

Generally, for graphene-based materials, weight loss at 100–350 ℃ is ascribed to the decomposition of the oxygen containing groups, while weight loss at ˃ 350 ℃ is ascribed to the bulk pyrolysis of the carbon skeleton [23]. Figure 5 shows the TG–DTA curves of MgO/GO, which comprised five distinct stages, as highlighted in different background colors. The first stage, $T < 100$ ℃, a slight weight loss of 1.98% and negative DTA value were ascribed to the evaporation of the water adsorbed on the sample surface. The second stage, 100 ℃ $< T <$ 350 ℃, weight loss of 11.83% and negative DTA value meant the endothermic decomposition of the labile oxygen-containing groups. The third stage, 350 ℃ $< T <$ 429 ℃, weight loss of 6.02% may be ascribed to the decomposition of the more stable oxygen-containing groups and pyrolysis of some carbon skeleton. The fourth stage, 429 ℃ $< T <$ 583 ℃, considerable weight loss of 68.41% and sharp DTA values meant the bulk pyrolysis of the carbon skeleton, which is an exothermic process. The fifth stage, T ˃ 583 ℃, DTA values were nearly zero, the weight percent went stabilized at 11.32%. The above analyses led us to determine the mass percent of the functional groups and MgO in MgO/GO as 17.85% and 11.32%, respectively.

Figure 6 compares the N$_2$ adsorption–desorption isotherms (a) and pore size distribution (b) of MgO, GO, and MgO/GO. All the three samples demonstrated

type V isotherm and type H3 hysteresis loop. These isotherm and hysteresis loop types commonly appear in either flaky or layered materials [24], which was in line with the layered graphene and flaky MgO exhibited in Fig. 2. The BET-specific surface area of MgO/GO was 172.70 m^2 g^{-1}, which was higher than that of either GO (163.35 m^2 g^{-1}) or MgO (8.30 m^2 g^{-1}). Besides, the average pore size of MgO, GO, and MgO/GO was 3.9, 3.7, and 2.1 nm, indicating a mesoporous feature.

pH$_{pzc}$ (point of zero charge) is the pH value under which the surface charge of the colloidal particles comes to zero. When pH < pH$_{pzc}$, the dominant H$^+$ will be massively adsorbed onto the surface of the colloidal particles to make zeta potential positive. On the contrary, when pH $^>$ pH$_{pzc}$, the dominant OH$^-$ will be massively adsorbed onto the surface of the colloidal particles to make zeta potential negative. Figure 7 shows the zeta potential of MgO/GO decreased with the increase in pH as expected and went to zero at the pH of 4, indicating that pH$_{pzc}$ of MgO/GO was 4.

Fig. 6 N$_2$ adsorption–desorption isotherms (**a**) and pore size distribution (**b**) of MgO, GO, and MgO/GO

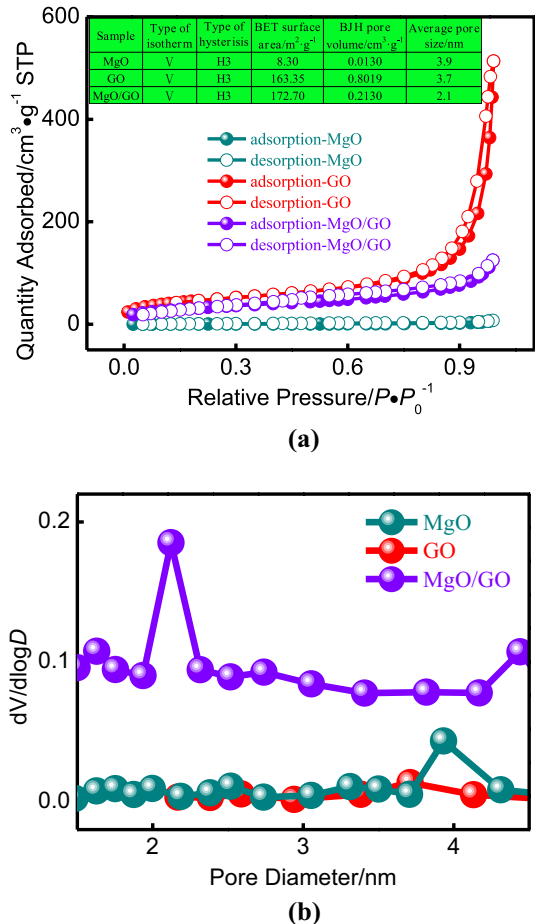| Sample	Type of isotherm	Type of hysterisis	BET surface area/m^2·g^{-1}	BJH pore volume/cm^3·g^{-1}	Average pore size/nm
MgO	V	H3	8.30	0.0130	3.9
GO	V	H3	163.35	0.8019	3.7
MgO/GO	V	H3	172.70	0.2130	2.1

(a)

(b)

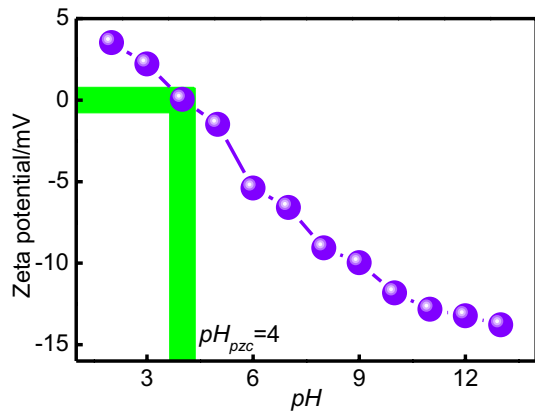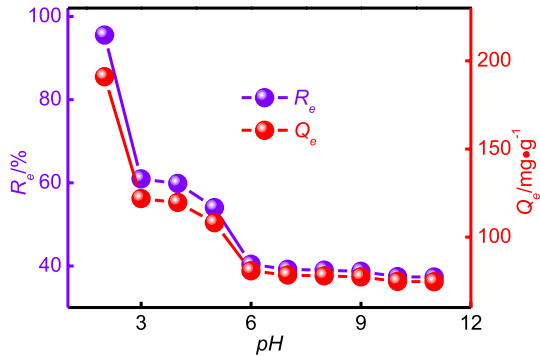**Fig. 7** Zeta potential of MgO/GO hydrosol at varying *pH*

Fig. 8 Effect of pH on the adsorption of CR by MgO/GO

Adsorption performance

Effect of pH

pH is a vital factor of adsorption. Figure 8 shows adsorption of CR decreased dramatically when pH was increasing in the range of 2–6. With the further increase in pH, adsorption changed slightly. When pH < 4 and ˃ 4, MgO/GO has positive and negative surface charges, respectively. Furthermore, CR is an anionic dye. When pH < 4, the electrostatic attraction between positive MgO/GO and negative CR was beneficial to adsorption. Thus, a high adsorption level was observed at pH = 2–3. As pH increased, the surface charge of MgO/GO decreased and went to zero when pH = 4. As a result, the electrostatic attraction between MgO/GO and CR was weakened, until turned to repulsion when pH exceeded 4. Thus, a remarkable decrease in adsorption was observed when pH increased from 2 to 6. As pH = 2 is a highly acidic thus corrosive condition, field application of MgO/GO may be conducted under the pH of 3, a less acidic pH at which the adsorption performance is still relatively high.

Effect of contact time

Contact time is a critical parameter that associates with the adsorption efficiency. Generally, adsorption rate is fast at the beginning and slows down with the lapse of contact time. This phenomenon can be understood from the aspects of adsorbate and adsorbent. (1) Adsorbate: At the beginning of adsorption, the adsorbate concentration, as well as the concentration gradient between the solution and adsorbent surface, is high. High concentration gradient enables fast diffusion. With the proceeding of adsorption, the concentration gradient decreases, leading to slowing down of adsorption. (2) Adsorbent: At the beginning of adsorption, many vacant adsorption sites on the adsorbent surface provide numerous collision opportunities for adsorbates. With the proceeding of adsorption, many adsorption sites become occupied, leading to the slow down of adsorption. Figure 9 exhibits the trends as expected. The adsorption is equilibrated at 10 min; the equilibrium adsorption capacity of MgO, GO, and MgO/GO was 124.92, 180.84, and 190.96 mg g^{-1}, respectively. The composite MgO/GO outperforms either MgO or GO, suggesting that a synergistic effect exists between them. The synergistic effect was originated from the interactions between MgO and GO in an atomic level, as confirmed by XRD, FTIR, and XPS analyses.

Effect of adsorbent dosage

Adsorbent dosage is a key parameter that determines the adsorption cost to a large extent. Generally, adsorption percent increases, while adsorption quantity decreases with the increase in adsorbent dosage. As adsorbent dosage increases, the adsorption sites in per unit volume increase, and the collision opportunities of adsorbates with adsorption sites increase accordingly, resulting in the increase in the adsorption percent. However, two disadvantages cause the decrease in adsorption quantity. (1) As adsorbent dosage increases, the dispersion is worsened, and some adsorption sites
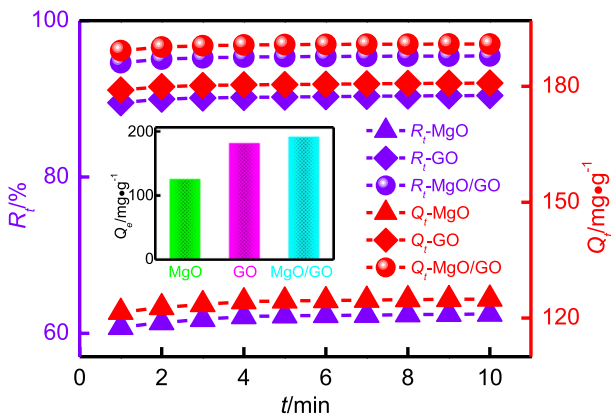

Fig. 9 Effect of contact time on the adsorption of CR by MgO, GO, and MgO/GO (inset: comparison of the equilibrium adsorption capacity of MgO, GO, and MgO/GO)

become unavailable. (2) As adsorbent dosage increases, the residue adsorbate concentration is consumed to a very low level. Figure 10 exhibits the changing trends of adsorption parameters with adsorbent dosage as expected. MgO/GO adsorbed ˃ 94% of CR in solution.

Effect of adsorbate initial concentration

A good adaptability to the initial concentration of adsorbate is essential to a potential adsorbent. Generally, adsorption percent decreases, while adsorption quantity increases with the increase in adsorbate initial concentration. On the one hand, as adsorbate initial concentration increases, the concentration gradient of adsorbates between the solution and adsorbent surface increases. The increasing concentration gradient facilitates adsorbates to diffuse toward adsorbent, resulting in the increase in the adsorption quantity. On the other hand, as adsorbate initial concentration increases, the collision probability between adsorbate and adsorbent increases, making more and more adsorption sites become occupied to reach a saturated state. As the adsorption sites are reaching saturation, the adsorption percent decreases. Figure 11 exhibits the changing trends of adsorption parameters with adsorbate initial concentration as predicted. MgO/GO maintained high adsorption percent for CR solutions of initial concentration 150–700 mg L^{-1}. Given the CR initial concentration 700 mg L^{-1}, the adsorption percent and quantity were 97.84% and 684.85 mg L^{-1}, respectively, indicating an excellent adaptability of MgO/GO to CR initial concentration.

Theoretical explanation of the effect of adsorbent dosage and adsorbate initial concentration on adsorption parameters

To establish a solid foundation for effecting rules of adsorbent dosage and adsorbate initial concentration on adsorption parameters, a theoretical explanation is given as follows. The parameters D, C_i, R_i, Q_i ($i = 0$, e, t) that appeared here have the same meanings as defined in Sect. 2.4.

From Eqs. (1)–(3) in Sect. 2.4, we derive:

Fig. 10 Effect of MgO/GO dosage on the adsorption of CR
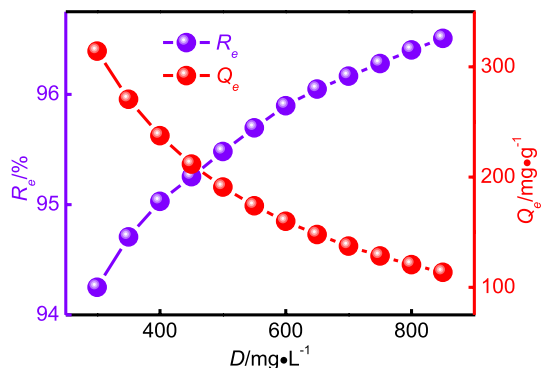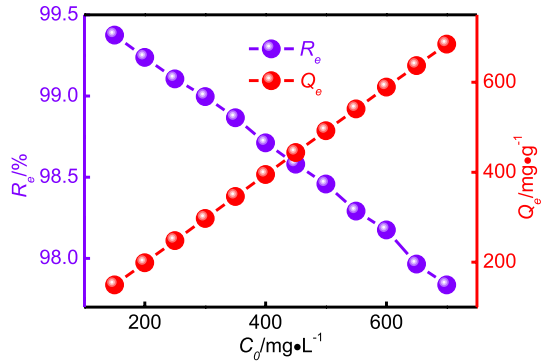
Fig. 11 Effect of CR initial concentration on its adsorption by MgO/GO

$$R_i = \frac{D \cdot Q_i}{C_0} \tag{4}$$

$$Q_i = \frac{C_0 \cdot R_i}{D} \tag{5}$$

From Eqs. (4) and (5), we can derive four partial differentials as follows:

$$\left(\frac{\partial R}{\partial D}\right)_{C_0} = \frac{Q_i}{C_0} \rangle 0 \tag{6}$$

$$\left(\frac{\partial Q_i}{\partial D}\right)_{C_0} = -R_i \cdot C_0 \cdot D^{-2} \langle 0 \tag{7}$$

$$\left(\frac{\partial R_i}{\partial C_0}\right)_D = -D \cdot Q_i \cdot C_0^{-2} \langle 0 \tag{8}$$

$$\left(\frac{\partial Q_i}{\partial C_0}\right)_D = \frac{R_i}{D} \rangle 0 \tag{9}$$

Equations (6) and (7) imply when adsorbate initial concentration is kept constant, adsorption percent and adsorption quantity increase and decrease with the increase in adsorbent dosage, respectively, as Fig. 10 displays.

Equations (8) and (9) imply when adsorbent dosage is kept constant, adsorption percent and adsorption quantity decrease and increase with the increase in adsorbate initial concentration, respectively, as Fig. 11 displays.

Effect of electrolyte

Various electrolytes commonly exist in the real wastewater, which may interfere with the adsorption conducted on the target contaminant. The overall effect of

electrolyte on adsorption is based on its effects on adsorbate, adsorbent, and the adsorption media, the three elements of an adsorption system. (1) Effect on adsorbate. ①Electrolytic ions compete for adsorption sites with ionic adsorbates (adverse effect). ②Electrolytic ions make aqueous adsorbates salt out (adverse effect). (2) Effect on adsorbent. Electrolytic ions neutralize the surface charge of adsorbent, bringing two consequences: ①The dispersion of adsorbent is worsened (adverse effect). ②The electrostatic interaction of adsorbent with ionic adsorbates is weakened (either adverse or beneficial effect). (3) Effect on adsorption media. The presence of electrolytic ions improves the electrical conductivity of the aqueous solution. As a result, the diffusion of ionic adsorbates either toward or backward adsorbent is facilitated (either adverse or beneficial effect).

In this work, we chose NaCl as an electrolyte representative for an investigation of the environmental adaptability of MgO/GO from one aspect. Figure 12 shows adsorption percent and adsorption quantity deceased slightly when NaCl concentration increased from 0 to 50 mmol L^{-1}, providing two implications: (1) The decrease in adsorption suggested that the adverse effects of NaCl on adsorption surpassed the beneficial ones. (2) The minor effect of NaCl on adsorption implied that CR may be closely attached onto MgO/GO surface via chemical interaction to form an inner sphere complex with compact structure [25]. The strong interaction between MgO/GO and CR made adsorption insensitive to electrolyte. However, more solid evidence is needed to support this speculation.

Cyclic adsorption performance

The reusability of an adsorbent is associated with cost control and also conforms well with the concept of circular economy. Yet, adsorbents suffer from performance decay due to increasing cycles. The performance decay is due to both energy loss and matter loss happened in adsorption–desorption cycles. (1) Energy loss. Adsorption sites of high affinity can hardly be released, making regeneration incomplete. (2) Matter loss. Firstly, adsorbent particles of high hydrophilicity can hardly be separated, making recovery incomplete. Secondly, the adsorbent may be transformed or even decomposed

Fig. 12 Effect of electrolyte on the adsorption of CR by MgO/GO
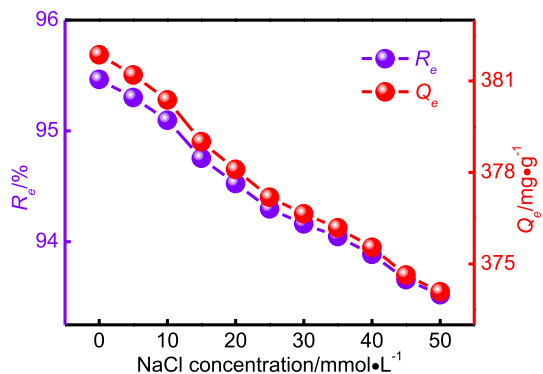
due to the change of the solution pH during adsorption–desorption cycles. Clearly, matter loss is associated with adsorbent stability to a higher extent than energy loss.

Figure 13 shows, after three and five consecutive cycles, the adsorption percent was 74.18% and 33.85%, exhibiting fair stability and reusability in three cycles. The change of the solution pH during adsorption–desorption cycles (adsorption pH=2, desorption pH=10) may impact MgO/GO stability in three levels: (1) Impact on MgO: Protonation–deprotonation changes the surface charge and crystal structure of MgO. (2) Impact on GO: Protonation–deprotonation changes the surface charge of GO, whereby changes the dispersibility of MgO/GO in solution. (3) Impact on MgO–GO interaction: As the FTIR analysis indicates, the MgO precursor interacted with the functional groups of GO such as –COOH to form MgO in situ. Consequently, the protonation–deprotonation cycles will definitely weaken the MgO–GO interaction, making the composite less stable.

Adsorption isotherms

The Langmuir model describes a monolayer adsorption on homogeneous surface sites with no interactions between adsorbed ions.

$$Q_e = Q_{max}K_LC_e/(1 + K_LC_e)$$

where Q_{max} (mg g^{-1}) denotes the monolayer adsorption capacity, K_L (L mg^{-1}) is the Langmuir adsorption constant relating to the adsorption heat. A separation or equilibrium factor R_L is defined as $R_L = 1/(1 + C_0K_L)$. When $0 < R_L < 1$ favorable adsorption is indicated, $R_L > 1$ means unfavorable adsorption, $R_L = 0$ means irreversible adsorption, and $R_L = 1$ means linear adsorption [26].

The equation for linearized form of Langmuir model is:
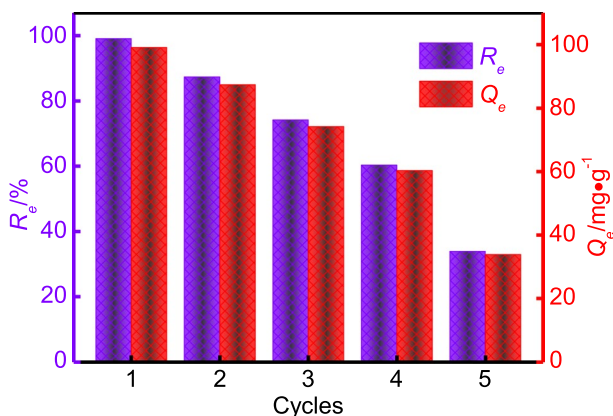
$$C_e/Q_e = 1/(K_LQ_{max}) = C_e/Q_{max}$$

Fig. 13 Cyclic adsorption performance of MgO/GO toward CR

The Freundlich model is widely used to describe adsorption on heterogeneous surface with varied adsorption heat.

$$Q_e = K_F C_e^{1/n}$$

where K_F and n are the Freundlich constants related to the adsorption capacity and adsorption intensity, respectively. The n parameter indicates whether the adsorption is a chemical process ($n < 1$) or a physical process ($n > 1$) [26].

The equation for linearized form of Freundlich model is:

$$\ln Q_e = \ln K_F = (1/n) \ln C_e$$

The Temkin model assumes that the adsorption heat caused by chemical interactions between adsorbent and adsorbate decreases linearly with coverage [27].

$$Q_e = (RT/A_T)(\ln B_T + \ln C_e)$$

where R (8.314 J mol^{-1} K^{-1}) is the gas constant, T (K) is the absolute temperature, A_T (J mol^{-1}) is a constant corresponding to the adsorption heat, B_T (L g^{-1}) is the equilibrium binding constant relating to the maximum binding energy.

The D–R model is used to identify the nature of an adsorption process via the value of the mean free energy of adsorption E (KJ mol^{-1}). The adsorption process is identified as physical adsorption if $E < 8$ kJ mol^{-1} and chemical adsorption if $8 < E < 16$ kJ mol^{-1} [28].

$$\ln Q_e = \ln Q_{max} - \beta \varepsilon^2 \quad \varepsilon = RT \ln[1 + (1/C_e)] \quad E = (2\beta)^{-0.5}$$

where Q_{max} is the theoretical maximum adsorption capacity, ε is the Polanyi potential, β (mol^2 J^{-2}) is a constant relating to E.

The fitting curves of the isotherm models are shown in Fig. 14; the fitting results are listed in Table 2. Table 2 presents the Freundlich model yielded R^2 of 0.9993, which was significantly higher than that of the other isotherm models. Moreover, the Freundlich constant $n = 0.4853$. The values of R^2 and n suggested that Freundlich model was suitable for describing the adsorption in equilibrium state, and adsorption is a favorable process classified as chemical adsorption on heterogeneous surface [26]. Herein, surface heterogeneity has three meanings: (1) heterogeneity at the geometric level, surface roughness, (2) heterogeneity at the phase level. MgO/GO consists of two different phases, MgO and GO, and (3) heterogeneity at energy level. Different functional groups such as carboxyl, hydroxy, carbonyl, epoxy have different affinities to adsorbate.

Adsorption kinetics

The pseudo-first-order (PFO) model assumes that the occupation rate of adsorption sites is proportional to the number of unoccupied sites [29].
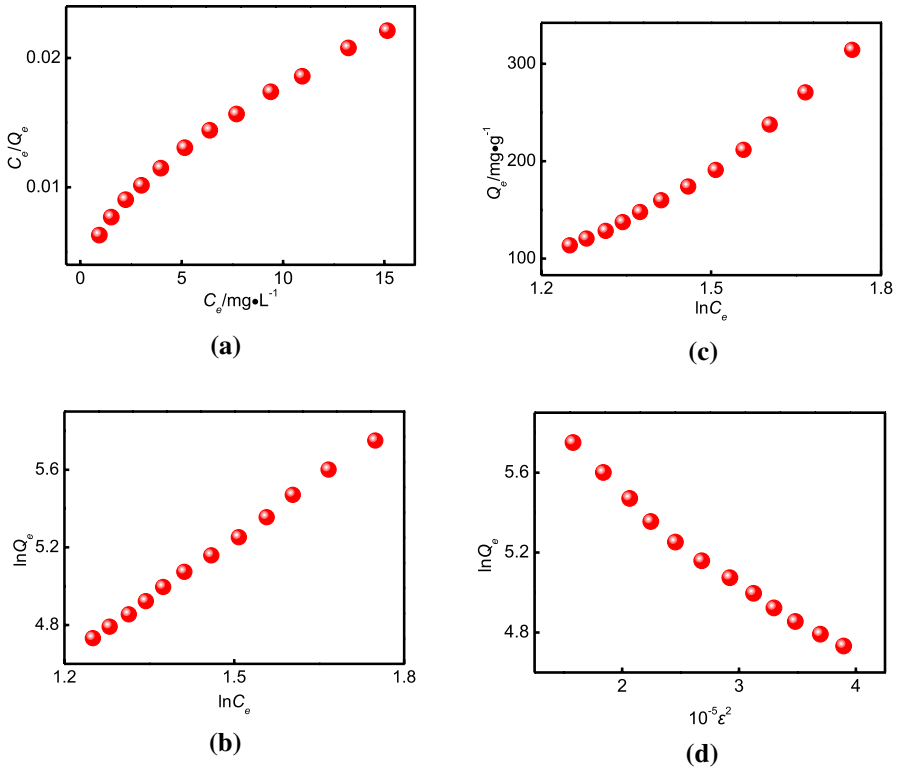
$$\ln(Q_e - Q_t) = \ln Q_e - k_1 t$$

Fig. 14 Fitting curves of the adsorption of CR by MgO/GO based on different isotherm models **a** Langmuir; **b** Freundlich; **c** Temkin; **d** D–R

where k_1 (min^{-1}) is the pseudo-first-order rate constant.

The pseudo-second-order (PSO) model assumes that the occupation rate of adsorption sites is proportional to the square of unoccupied sites, and chemisorption is the rate-controlling step [29].

$$t/Q_t = [1/k_2 Q_e^2)] = (t/Q_e)$$

where k_2 (g mg^{-1} min^{-1}) is the pseudo-second-order rate constant.

The intra-particle diffusion model is based on the theory developed by Weber and Morris [30]. If the fitting curve of Q_t versus $t^{0.5}$ is linear, then intra-particle diffusion is involved in the adsorption process. Moreover, if the linear fitting curve passes through the origin, then intra-particle diffusion is the only rate-controlling step, if not, then not the only rate-limiting step.

$$Q_t = k_{id}t^{0.5} + C$$

where k_{id} (mg g^{-1} min$^{-0.5}$) is the intra-particle diffusion rate constant, C (mg g^{-1}) is a constant related to the thickness of the boundary layer.

Table 2 Fitting and calculation results of CR adsorption by MgO/GO

Types	Models	Parameters			R^2
Isotherm	Langmuir	Q_{max}/mg g^{-1}	K_L/L mg^{-1}	R_L	0.9785
		917.4312	0.1634	0.0240	
	Freundlich	n	K_F		0.9993
		0.4853	8.6249		
	Temkin	A_T/J mol^{-1}	B_T/L g^{-1}		0.9779
		6.2830	0.3701		
	D-R	Q_{max}/mg g^{-1}	E/J mol^{-1}		0.9848
		581.8659	339.5665		
Kinetics	Pseudo-first-order	k_1/min^{-1}	Q_e/mg g^{-1}		0.9818
		0.3995	1.8962		
	Pseudo-second-order	k_2/g (mg min)$^{-1}$	Q_e/mg g^{-1}		0.9999
		0.6838	191.2046		
	Intra-particle diffusion	K_{id1}/mg/(g min$^{0.5}$)	C_1/mg g^{-1}		
		2.1586	187.0893		
		K_{id2}/mg/(g min$^{0.5}$)	C_2/mg g^{-1}		0.9425
		0.7848	189.0768		
		K_{id3}/mg/(g min$^{0.5}$)	C_3/mg g^{-1}		0.9659
		0.1957	190.3555		
	Liquid film diffusion	k_{fd}			0.9818
		0.3995			
	Bangham	α	k_0		0.9002
		0.0037	0.0383		

Thermo-dynamics	Van't Hoff	T/K	K^Θ	ΔH/kJ mol^{-1}	ΔS/J K^{-1} mol^{-1}	ΔG/kJ mol^{-1}	
		278.15	31.2528	10.0395	64.7113	−7.9600	
		283.15	33.7470			−8.2835	
		288.15	36.3350			−8.6071	
		293.15	39.0201			−8.9306	0.9999
		298.15	41.8363			−9.2542	
		303.15	44.7167			−9.5777	
		308.15	47.6998			−9.9013	
		313.15	50.7705			−10.2249	

For the liquid film diffusion model, if the fitting curve of $\ln[1 - (Q_t/Q_e]$ versus t is linear and pass through the origin, then liquid film diffusion is the rate-controlling step [31].

$$\ln[1 - (Q_t/Q_e)] = -k_{fd}t$$

where k_{fd} is the liquid film diffusion rate constant.

The Bangham model suggests pore diffusion mechanism when the R^2 of the fitting curve is higher than 0.99 [27].

$$\log\{\log[C_0/C_0 - Q_t \cdot m)]\} = \log(K_0 m/2.303V) + \alpha \log t$$

where m (g) is the mass of adsorbent, V (L) is the volume of the adsorbate solution, k_0 and α are constants.

The fitting curves of the kinetic models are shown in Fig. 15; the fitting results are listed in Table 2. The PSO model yielded R^2 of 0.9999, which was remarkably higher than that of the other kinetic models. Moreover, the adsorption capacity as calculated by the PSO model was 191.20 mg g^{-1}, which was in good agreement with the experimental value 190.96 mg g^{-1}. The high R^2 and the good agreement of fitting result with the experimental value indicated the suitability of PSO model in describing the adsorption in non-equilibrium state. Resultantly, the excellent fitting of adsorption to the PSO model has two implications: (1) Adsorption was mainly based on chemical interactions. (2) Chemical adsorption was the rate-controlling step [29]. The fitting curve of the intra-particle diffusion model exhibited three consecutive stages with declining rates (as highlighted in cyan, green, and yellow background colors in Fig. 15c). These three stages were film diffusion, pore diffusion, and surface reaction [32]. As having the slowest rate, surface reaction was the rate-controlling step, which coincided with PSO model. Furthermore, the liquid film diffusion model and the Bangham model did not yield satisfactory R^2, implying that neither liquid film diffusion nor pore diffusion was the rate-controlling step. Evidently, the fast pore diffusion was owing to the thin morphology that enabled short diffusion path. Since both film diffusion and pore diffusion were quite fast (Fig. 15c), the adsorption rate was controlled solely by surface reaction, resulting in a fast overall kinetics (Fig. 9).

Adsorption thermodynamics

The thermodynamic functions were evaluated based on the Van't Hoff equation:

$$\ln K^\ominus = \frac{-\Delta G}{RT} = \frac{-\Delta H}{RT} + \frac{\Delta S}{R}$$

$$K^\ominus = \frac{Q_e}{C_e}$$

where $K^\ominus$ (L g^{-1}) is the adsorption equilibrium constant, ΔG (KJ mol^{-1}) is the adsorption free energy change, ΔH (KJ mol^{-1}) is the adsorption enthalpy change, ΔS (J K^{-1} mol^{-1}) is the adsorption entropy change.

The fitting curve of the Van't Hoff equation is shown in Fig. 16; the fitting results are listed in Table 2. The thermodynamic functions were $\Delta G < 0$, $\Delta H > 0$, and $\Delta S > 0$, which indicated that adsorption was a spontaneous, endothermic, and randomness increasing process [26, 33]. During adsorption, CR replaces the water molecules on the MgO/GO surface, leading to the entropy increase in the water molecules and
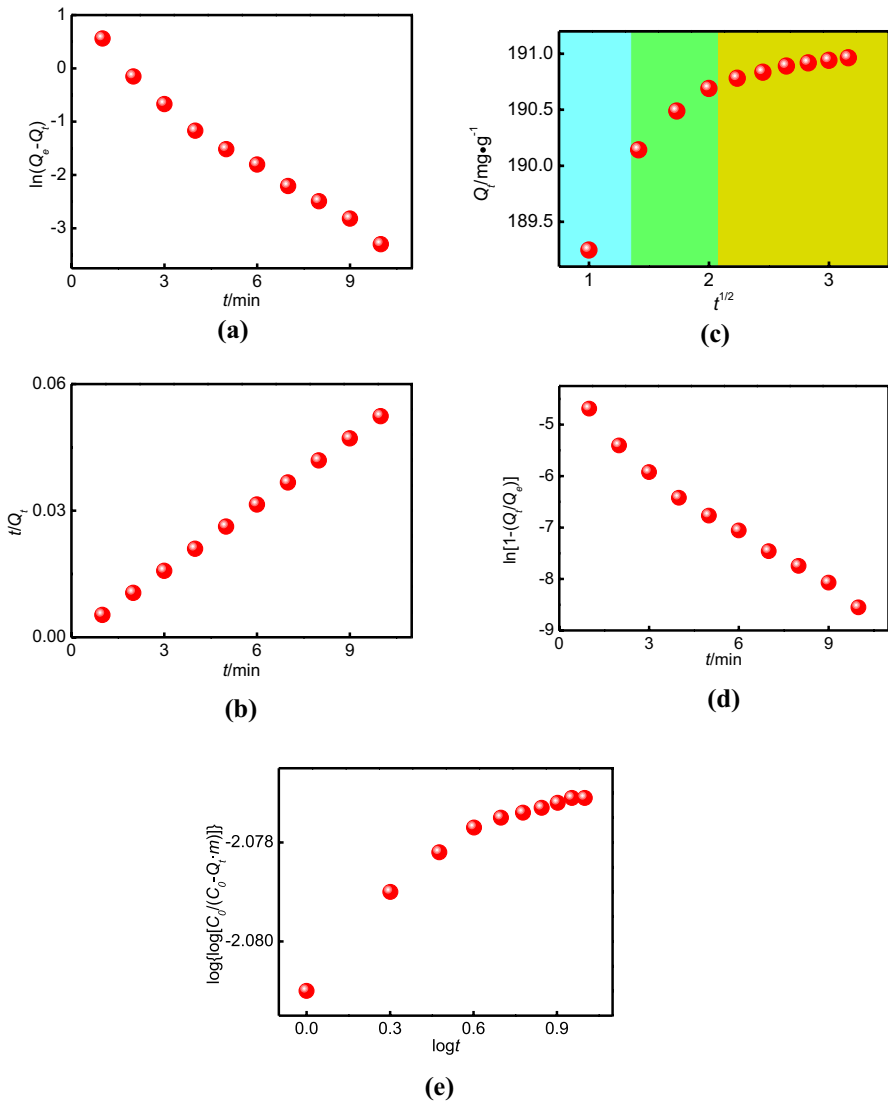
Fig. 15 Fitting curves of the adsorption of CR by MgO/GO based on different kinetic models **a** Pseudo-first-order, **b** Pseudo-second-order, **c** Intra-particle diffusion (The cyan, green, and yellow area indicate film diffusion, pore diffusion, and surface reaction as the three consecutive stages in typical chemisorption, respectively). **D** Liquid film diffusion, **e** Bangham

entropy decrease of CR. Clearly, the former prevailed over the latter to make $\Delta S > 0$ [34].

Besides, ΔG became more negative as the temperature increased. A more negative ΔG means an improved thermodynamic spontaneity [26]. Increasing

Fig. 16 **a** Equilibrium curves under varying temperatures of CR adsorption by MgO/GO, **b** fitting curve of CR adsorption by MgO/GO based on Van't Hoff equation

(a)

(b)
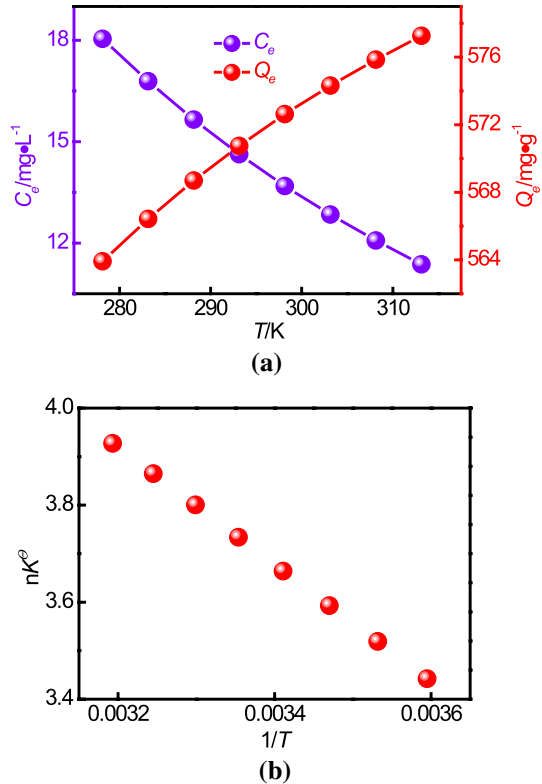
temperature enhances the ionization of the functional groups to form more adsorption sites, resulting in the improvement of the adsorption spontaneity.

Interaction mechanism

The FTIR and UV–Vis spectra of the sample before (MgO/GO) and after (MgO/GO-CR) adsorption were compared to shed light on the interaction mechanism. Figure 3 shows, in the FTIR spectrum of MgO/GO-CR, the peak at 1458 cm^{-1} was ascribed to the vibration of benzene ring [35]. The appearance of benzene peak confirmed the adsorption of CR onto MgO/GO. Peaks of MgO/GO and CR suffered from several changes due to adsorption as follows. (1) O–H peak of MgO/GO. Change of peak position: blue shifted, change of peak intensity: weakened. Generally, formation of hydrogen bond leads to the decrease in the electron density, thus making FTIR peak red shift. As Fig. 8 reveals, electrostatic attraction exists between MgO/GO and CR when pH = 2, the optimized pH under which the batch adsorptions were conducted. Yet, O–H peak blue shifted, which implied that O–H was involved in CR adsorption via electrostatic attraction, rather than hydrogen bond. (2) C–OH peak of MgO/GO. Peak intensity was weakened. (3) C=C peak of MgO/GO. Change of peak position: red shifted, change of peak

intensity: strengthened. These changes implied that MgO/GO and CR acted upon each other via face-to-face π–π interaction rather than edge-to-face one to form a bigger conjugated system. (4) Mg–OH peak of MgO/GO. Both the peak position and intensity changed slightly after adsorption, which implied that MgO may participate in CR adsorption via weak van der Waals force. (5) Benzene peaks of CR. Two benzene peaks at 1498 cm^{-1} and 1583 cm^{-1} became one peak at 1458 cm^{-1} due to adsorption. This implied π–π interaction between MgO/GO and CR.

For the UV–Vis spectra of aromatic compounds, π→π* and n→π* peaks come from the transition of π electrons and lone pair electrons to anti-bonding orbital π*, respectively. So, π→π* and n→π* peaks are the signals of nonpolar conjugate carbon atoms and polar functional groups, respectively. Generally, polarity increase causes π→π* red shift and n→π* blue shift. On the contrary, polarity decrease causes π→π* blue shift and n→π* red shift. Figure 17 shows the π→π* and n→π* peaks of MgO/GO red shifted and blue shifted, respectively, and peaks intensity weakened significantly after CR adsorption. These changes can be understood as follows: (1) The formation of inner sphere complexes via chemical interaction between MgO/GO and CR (as speculated from Fig. 12) led to the polarity increase in MgO/GO, as CR is an ionic dye having high polarity. (2) The change of π→π* peak indicated π–π interaction between MgO/GO and CR, which was consistent with FTIR analysis. (3) The change of n→π* peak indicated electrostatic interaction between MgO/GO and CR, which also coincided with FTIR analysis.

The above analyses led us to draw a conclusion on the adsorption mechanism: Both GO and MgO participated in CR adsorption. GO adsorbed CR via electrostatic attraction and face-to-face π–π interaction. MgO adsorbed CR via weak van der Waals force. This conclusion was in well accordance with those derived from the batch adsorptions, adsorption isotherms, and adsorption kinetics. The proposed interaction mechanism between MgO/GO and CR is illustrated in Scheme 2.

**Fig. 17** UV–Vis spectra of MgO/GO and MgO/GO-CR
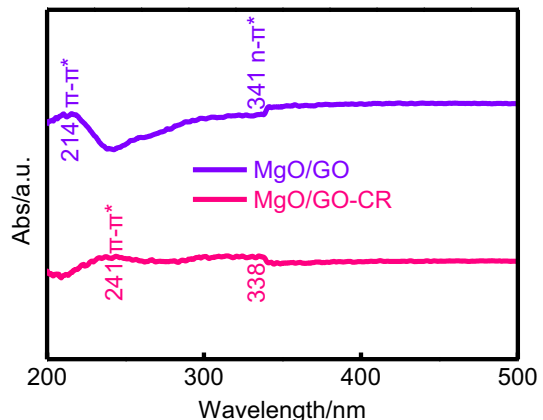
Performance evaluation

The adsorption performance of MgO/GO was evaluated by comparing with other adsorbents in initial concentration (C_0), dosage (D), equilibrium time (t_e), and adsorption capacity (Q_{max}), which are exhibited in Table 3. Clearly, MgO/GO has shorter equilibrium time and fair adsorption capacity. Therefore, MgO/GO is superior in adsorption efficiency.

Conclusion

MgO/GO was prepared and used to remove aqueous CR. The adsorption of CR (initial concentration 700 mg L^{-1}) onto MgO/GO (dosage 1000 mg L^{-1}) equilibrated in 10 min, adsorption percent and adsorption quantity were 97.84% and 684.85 mg g^{-1}, respectively. Meanwhile, the adsorption adapted well to the fluctuations of environmental factors including dye concentration and coexisting electrolyte. The adsorption fits well with the PSO model and Freundlich model; chemical adsorption was the rate-controlling step. As for interaction mechanism, GO component adsorbed CR via electrostatic attraction and face-to-face π–π interaction, while MgO component adsorbed CR via weak van der Waals force. The advantages of facile preparation, high adsorption efficiency, and good environmental adaptability may enable MgO/GO to be a promising adsorbent for aqueous dyes.
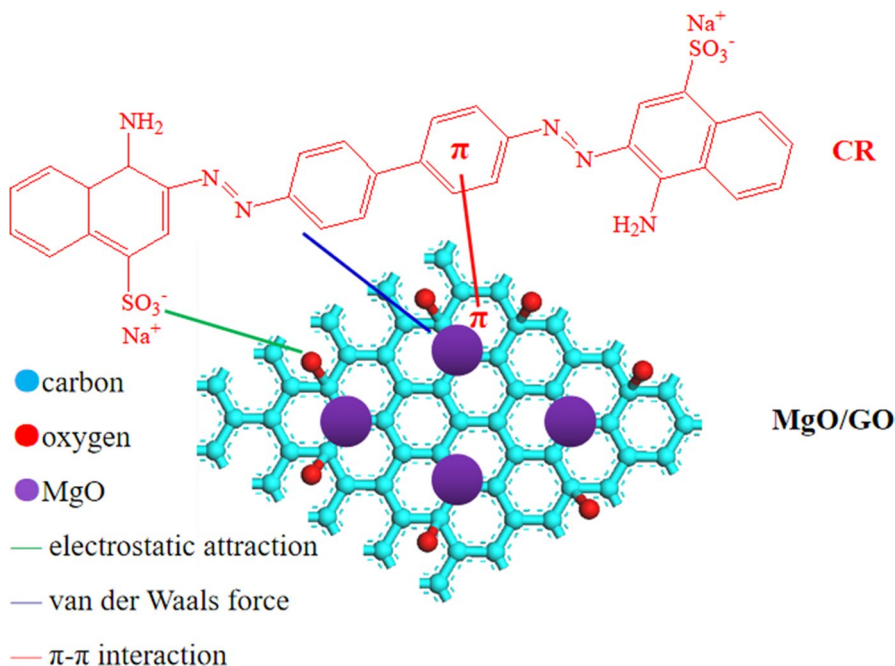
Scheme 2 Proposed interaction mechanism between MgO/GO and CR

Table 3 Comparison of the adsorption performance of MgO/GO with other adsorbents

Adsorbent	Adsorbate	C_0/mg L^{-1}	D/mg L^{-1}	t_e/min	Q_{max}/mg g^{-1}	Cycles	R_e/%	Ref
C/NiO–ZnO	CR	50	500		613	5	97.9	[1]
NiO–ZnO	CR				534.00			[1]
Carbon	CR				167.00			[1]
MgO	CR	500	1250	30	1928.00			[11]
MgO	CR	50	200	200	227.7			[16]
MgO-GO	CR	50	200	200	237.0			[16]
Porous NiCo$_2$O$_4$ nanosheets	CR	360	200		961.50			[35]
FexCo$_{3-x}$O$_4$ nanoparticles	CR	30	100	240	128.60	5	100.00	[36]
Three-dimensional Cd$_4$(H$_4$L)$_2$(phen)$_2$(H$_2$O)$_4$	CR	100	333	60	684.00			[37]
GO/Fe$_3$O$_4$	CR	100	500	120	628.93	5	87.23	[38]
Hierarchical magnetic carbon nanosheet	CR	200	500	120	724.00	6		[39]
3D hierarchical graphene oxide-NiFe LDH	CR			225	489	4	74.20	[40]
Graphene oxide	CR	100	1200	120	120.20	5	91	[41]
MgO/GO	CR	700	1000	10	684.85	5	33.85	This work

Authors' promise about complying with Springer's ethical standards

The authors can assure to comply with Springer's ethical standards. The manuscript which is being submitted to **Research on Chemical Intermediates** has not been published previously in any form. Authors also assure that the manuscript is not under consideration for publication elsewhere and that its publication is approved by all authors and tacitly or explicitly by the responsible authorities where the work was carried out. The authors declare that they have no known competing financial interests or personal relationships that could have appeared to influence the work reported in this paper. The authors also declare that no research involving human participants and/or animals was implemented in this work. Each author knew that the submission also implies that, if accepted, it will not be published elsewhere in the same form, in English or in any other language, without the written consent of the copyright holder.

Author contributions Ting Guo was involved in formal analysis, investigation, data curation, supervision, validation, and project administration. Chaoke Bulin performed conceptualization, writing—original draft, writing—review & editing, visualization, resources, and funding acquisition.

References

1. H. Chen, S. Wageh, A. Al-Ghamdi, H.Y. Wang, J.G. Yu, C.J. Jiang, J. Colloid Interface Sci. **537** (2019).
2. N.S. Shah, J.A. Khan, M. Sayed, Z.H. Khan, J. Iqbal, S. Arshad, M. Junaid, H.M. Khan, Sep. Purif. Technol. **233**, 115966 (2020)
3. F.U. Nigiz, Res Chem Intermed. **45** (2019).
4. J.M. Pan, J. Ren, Y. Xie, X.S. Wei, Y. Guan, X.H. Yan, H. Tang, X.N. Cheng, Res Chem Intermed. **43** (2017).
5. J. Dotto, M.R.F. Klen, M.T. Veit, S.M. Palácio, R. Bergamasco, J. Cleaner Prod. **208** (2019).
6. G.J. Rani, M.A.J. Rajan, G.G. Kumar, Res Chem Intermed. **43** (2017).
7. P.P.A. Jose, M.S. Kala, N. Kalarikkal, S. Thomas, Res Chem Intermed. **44** (2018).
8. M. Kovacic, J. Papac, H. Kusic, P. Karamanis, A.L. Bozic, Chem. Eng. J. **382**, 122826 (2020)
9. G.B. Li, H. Liang, Chem. Eng. J. **382**, 122919 (2020)
10. Z.W. Xu, Y.Y. Zhang, X.M. Qian, J. Shi, L. Chen, B.D. Li, J.R. Niu, L.S. Liu, Appl. Surf. Sci. **316** (2014).
11. X.L. Wu, Y.P. Shi, S.X. Zhong, H.J. Lin, J.R. Chen, Appl. Surf. Sci. **378** (2016).
12. M.M. Gao, Z.M. Wang, C.X. Yang, J.L. Ning, Z.D. Zhou, G.Y. Li, Colloids Surf., A. **566** (2019).
13. R. Soni, D.P. Shukla, Chemosphere **219** (2019).
14. V.P. Santos, L. Borges, S. Sartipi, B.D. Linden, A. Iulian, Dugulan, A. Chojecki, T. Davidian, M. Ruitenbeek, G.R. Meima, F. Kapteijn, M. Makkee, J. Gascon, Appl. Catal., A. **533** (2017).
15. K. Ahmad, S.M. Mobin, J. Environ. Chem. Eng. **7**, 103347 (2019)
16. J. Xu, D.F. Xu, B.C. Zhu, B. Cheng, C.J. Jiang, Appl. Surf. Sci. **435** (2018).
17. M. Nagpal, R. Kakkar, Res. Chem. Intermed. **s11164** (2020).
18. S.K. Sahoo, G. Hota, J. Environ. Chem. Eng. **6** (2018).
19. S.K. Sahoo, J.P. Dhal, G.K. Panigrahi, Composites Communications **22** (2020).
20. S.K. Sahoo, S. Padhiari, S.K. Biswal, B.B. Panda, G. Hota, Mater. Chem. Phys. **244** (2020).

21. H.T. Yu, B.W. Zhang, C.K. Bulin, R.H. Li, R.G. Xing, Sci. Rep. **6**, 36143 (2016)
22. M. Moradi, G. Moussavi, K. Yaghmaeian, A. Yazdanbakhsh, V. Srivastava, M. Sillanpää, Appl. Catal., B. **260**, 118128 (2020).
23. Y.J. Yao, S.D. Miao, S.Z. Liu, L.P. Ma, H.Q. Sun, S.B. Wang, Chem. Eng. J. **184** (2012).
24. C.P. Kong, M. Li, J.C. Li, X.J. Ma, C.P. Feng, X. Liu, RSC Adv. **9** (2019).
25. Q.S. Hu, Y.L. Liu, X.Y. Gu, Y.P. Zhao, Chemosphere **181** (2017).
26. Q.W. Zhou, B.H. Liao, L.N. Lin, W.W. Qiu, Z.G. Song, Sci. Total Environ. **615** (2018).
27. E. Wibowo, M. Rokhmat, Sutisna, Khairurrijal, M. Abdullah, Desalination **409** (2017).
28. T.A. Saleh, A. Sari, M. Tuzen, Chem. Eng. J. **307** (2017).
29. Y.C. Qi, M.L. Yang, W.H. Xu, S. He, Y. Men, J. Colloid Interface Sci. **486** (2017).
30. W.J. Weber, J.C. Morris, J Sanit Eng Div. **89** (1963).
31. S.A. Chaudhry, Z. Zaidi, S.I. Siddiqui, J. Mol. Liq. **229** (2017).
32. K.L. Tan, B.H. Hameed, J. Taiwan Inst. Chem. Eng. **74** (2017).
33. F. Hayeeye, M. Sattar, W. Chinpa, O. Sirichote, Colloids Surf., A. **513** (2017).
34. Y.J. Li, W.F. Li, Q.N. Liu, H. Meng, Y.Z. Lu, C.X. Li, J. Environ. Sci. **68** (2018).
35. Y.Q. Bao, M. Qin, Y.K. Yu, L. Zhang, H.J. Wu, J. Phys. Chem. Solids. **124** (2019).
36. J. Liu, N. Wang, H.L. Zhang, J. Baeyens, J. Environ. Manage. **238** (2019).
37. J. Ai, H.R. Tian, X. Min , Z.C. Wang, Z.M. Sun, Dalton Trans. **49** (2020).
38. S.Y. Pu, S.Y. Xue, Z. Yang, Y.Q. Hou, R.X.n Zhu, W. Chu, Environ. Sci. Pollut. Res. **25** (2018).
39. Y. Shen, L. Li, Z.H. Zhang, J. Phys. Chem. C. **120** (2016).
40. Y.Q. Zheng, B. Cheng, W. You, J.G. Yu, W.K. Ho, J. Hazard. Mater. **369** (2019).
41. S.K. Sahoo, J.K. Sahoo, G.K. Panigrahi, D.K. Pattanayak, A.S. Rout, A. Lenka, FlatChem. **24** (2020).